

**Atomic photoionization by spatiotemporal optical vortex pulses**Yongkun Chen <sup>1</sup>, Yueming Zhou <sup>1,\*</sup>, Min Li <sup>1</sup>, Kunlong Liu <sup>1</sup>, Marcelo F. Ciappina <sup>2,3,4,†</sup> and Peixiang Lu<sup>1,5</sup><sup>1</sup>*School of Physics and Wuhan National Laboratory for Optoelectronics, Huazhong University of Science and Technology, Wuhan 430074, China*<sup>2</sup>*Department of Physics, Guangdong Technion—Israel Institute of Technology, 241 Daxue Road, Shantou, Guangdong 515063, China*<sup>3</sup>*Technion—Israel Institute of Technology, Haifa, 32000, Israel*<sup>4</sup>*Guangdong Provincial Key Laboratory of Materials and Technologies for Energy Conversion, Guangdong Technion—Israel Institute of Technology, 241 Daxue Road, Shantou, Guangdong 515063, China*<sup>5</sup>*Optics Valley Laboratory, Wuhan 430074, China*

(Received 5 December 2022; accepted 8 March 2023; published 20 March 2023)

Electromagnetic waves with a helical-like wavefront are known as optical vortices. One of their main characteristics is a phase structure that has a circulation around a singularity and that they carry orbital angular momentum (OAM). OAM is a fundamental property that governs the interaction of these sources with matter. In the present paper, we study the electron dynamics driven by a so-called spatiotemporal optical vortex (STOV). Contrary to the conventional optical vortices, a STOV carries transverse OAM. By designing a streakinglike technique, we aim to fully characterize the OAM of the STOV. Using both quantum mechanical and semiclassical models, we are able to dissect the spatially resolved photoelectron energy spectra and accurately retrieve the OAM. Our approach paves the way toward a complete understanding of the interaction of complex spatiotemporal light fields with atomic targets.

DOI: [10.1103/PhysRevA.107.033112](https://doi.org/10.1103/PhysRevA.107.033112)**I. INTRODUCTION**

Light with a helical wavefront or phase structure configures what is known as an optical vortex [1]. This phase has a circulation around a phase singularity, where the field amplitude vanishes and the azimuthal phase is discontinuous. In an optical vortex, the light field carries an orbital angular momentum (OAM) of  $l\hbar$  per photon ( $l$  is known as the topological charge). Typically, Laguerre-Gauss [2] or Bessel-Gauss [3] models are used to deal with optical vortices. Light fields with OAM have been widely studied [4–10] and applied in many areas, such as microscopy [11], optical communication [12], and particle tweezing [13] to cite just a few. Very recently, schemes with time-varying OAM were also introduced [14,15].

In laser-matter interaction processes, the conservation of OAM has been extensively examined. Previous work pointed out that the transfer of OAM from the photon to the atomic system would induce nondipole transitions [16,17], and this has been observed experimentally in quadrupole electronic excitations [18]. Meanwhile, the effect of OAM on the photoelectrons distribution has been investigated theoretically [19–23]. However, as the field amplitude vanishes at the phase singularity, the measured observables are dominated by those electrons released in areas where the laser has higher intensity, thus the transfer of OAM appears to be negligible [24].

Furthermore, either by XUV photoionization in the presence of an optical vortex pulse [25–27] or taking advantage of the spin-orbit interaction [28,29], the transfer of OAM in strong field ionization was experimentally implemented. In high-order harmonic generation (HHG), the harmonics flux results from the coherent superposition contribution of phase-matched single-atom responses, carrying phase information over the entire region of the optical vortex. Thus, the OAM transfer from the infrared (IR) photon to their harmonics is easy to achieve. In this way, the production of attosecond pulses with tuneable OAM becomes feasible [30–34].

Whether we use a Laguerre-Gauss or Bessel-Gauss model, the OAM vector is parallel to the light propagation direction, namely, it is longitudinal. A few years ago, a concept, coined spatiotemporal optical vortex (STOV), carrying a transverse OAM, i.e., the OAM vector is perpendicular to the propagation direction, was proposed [35–37]. A STOV is essentially a polychromatic electromagnetic structure, with phase circulation in the spatiotemporal plane. STOVs were first observed from short pulse filamentation in air [38] and were recently generated successfully in free space [39,40]. Subsequently, an accurate theoretical description of the propagation, polarization, and angular-momentum properties of a Bessel-type pulse STOV, as well as its scalar and vector spatiotemporal Bessel-type solutions, was introduced in Ref. [41]. It should be noted that the expected value of the transverse OAM depends not only on the topological charge  $l$  but also on the group velocity dispersion and the spatiotemporal eccentricity of the STOV pulse [42]. Similar to traditional optical vortices, the conservation of transverse OAM in laser-matter interaction processes driven by a STOV has also been investigated. Likewise,

\*Corresponding author: [zhouymhust@hust.edu.cn](mailto:zhouymhust@hust.edu.cn)†Corresponding author: [marcelo.ciappina@gtit.edu.cn](mailto:marcelo.ciappina@gtit.edu.cn)

recent work explored the conservation and characterization of transverse OAM in second harmonic generation [43,44]. In HHG, the transverse OAM of the high-order harmonics can be controlled through a two-color counterspin and counter-roticity STOV pulse. Furthermore, it was also found that spatially resolved harmonic spectra present an interference pattern caused by the spatiotemporal phase singularity [45]. Besides all these investigations, it is not clear how transverse OAM is transferred in other strong-field processes.

In this contribution, we theoretically study atomic photoionization driven by STOV pulses. In our prototypical scheme, an H atom is ionized by a STOV with a central wavelength of 1600 nm, assisted by an XUV pulse. By changing the spatial location and time delay of the XUV pulse relative to the STOV, the strong field ionization can be controlled in space and time, respectively. To simulate the electron dynamics, we numerically solve the three-dimensional time-dependent Schrödinger equation (3D-TDSE). From the time-propagated electron wave function, we calculate the photoelectron momentum distribution (PMD) and the energy spectra for different positions and time delays. We show that the photoelectron energy spectra depend on the spatial location of the XUV pulse and exhibit distinct interference patterns. The former reflects the spatial chirp of the electric field of the STOV pulse, which is traced back to the spatiotemporal phase circulation [45]. The latter is due to the presence of the spatiotemporal singularity, which makes the electrons ionized before and after such singularity interfere with each other. By employing the strong field approximation (SFA) [46,47], we reproduce the interference pattern from a classical trajectory-based perspective and demonstrate its physical origin. In addition, through the interference fringes, the OAM of the STOV can be fully characterized. Here, as the OAM increases, the fringes become denser. Our results provide a method to study STOV using photoelectrons and extend its application to strong-field ionization.

## II. NUMERICAL METHODS

The electric field of a linearly polarized STOV, propagating along the  $z$  axis and carrying an OAM with topological charge  $l$ , can be described mathematically as [38,40,43,45] (atomic units are used throughout unless stated otherwise)

$$\begin{aligned} \mathbf{F}_{\text{ST}}^l(t, x, y, z) = & F_0^{\text{ST}} \alpha_0 \left[ \left( \frac{x}{w_x} \right)^2 + \left( \frac{t - \frac{z}{v_g}}{w_t} \right)^2 \right]^{\frac{|l|}{2}} \\ & \times \exp \left[ - \left( \frac{x}{w_x} \right)^2 - \left( \frac{y}{w_y} \right)^2 - d \left( \frac{t - \frac{z}{v_g}}{w_t} \right)^2 \right] \\ & \times \exp[i(\omega_{\text{ST}} t - k_{\text{ST}} z - l \phi_{\text{ST}})] \hat{x}. \end{aligned} \quad (1)$$

Here, the OAM vector is along the  $y$  axis,  $(t, x, y, z)$  are the spatiotemporal coordinates;  $\hat{x}$  is the polarization direction;  $F_0^{\text{ST}}$  is the electric field peak amplitude;  $\alpha_0 = [2e/|l|]^{|l|/2}$  is a normalization constant;  $v_g = c$  is the light group velocity;  $w_x$ ,  $w_y$ , and  $w_t$  are the spatial and temporal scale widths, respectively;  $k_{\text{ST}}$  is the wave number;  $\omega_{\text{ST}}$  is the central

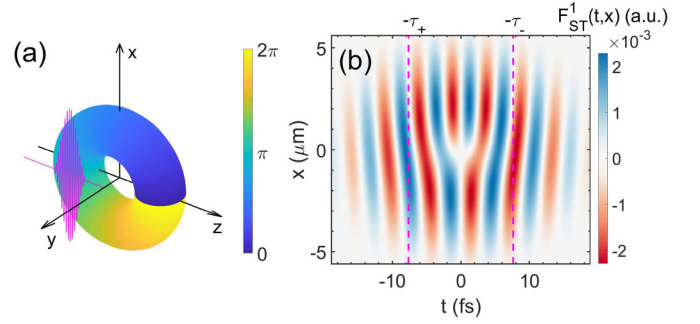


FIG. 1. (a) Schematic representation of the propagation of a STOV pulse with  $l = 1$ . The dashed violet curve represents an XUV pulse located at  $x = 0$  and a positive time delay relative to the spatiotemporal singularity. (b) Spatiotemporal distribution of the electric field of the STOV with  $l = 1$  at  $z = y = 0$ . The dashed violet lines denote the position of the XUV pulse in the space-time plane ( $x - z$  plane). The time delay is chosen to be before ( $\tau_+ = w_t \sqrt{|l|/2}$ ) or after ( $\tau_- = -w_t \sqrt{|l|/2}$ ) the spatiotemporal singularity, and the  $x$  position is scanned from  $-1.6 w_x \sqrt{|l|/2}$  to  $1.6 w_x \sqrt{|l|/2}$ .

frequency; and  $\phi_{\text{ST}} = \tan^{-1}[\frac{xw_t}{(t-z/v_g)w_x}]$  is the spatiotemporal phase. Here,  $\phi_{\text{ST}}$  means that the phase circulates in the  $x-z$  plane and rotates about the  $y$  axis. Considering that the OAM vector is directed along the  $y$  axis, only the  $y$  component of the transverse OAM exists. The corresponding angular momentum operator can be written as  $L_y = -i(v_g t - z) \frac{\partial}{\partial x}$ , with an expected value  $\langle L_y \rangle = l/2$  [42]. Note that it will not play any role in our study. In Fig. 1(a), we show a STOV pulse with  $l = 1$ , joint with the assisting XUV pulse (see below for more details). The STOV pulse appears as a flying donut with transverse OAM. Around the spatiotemporal singularity of the donut center, the phase of the STOV has a  $2\pi$  circulation (for  $l = 1$ ). In Fig. 1(b), the spatiotemporal distribution of the STOV electric field with  $l = 1$  at  $z = y = 0$  is shown. In this work, a STOV pulse with wavelength  $\lambda_{\text{ST}} = 1600$  nm and intensity  $I_{\text{ST}} = 1 \times 10^{12}$  W/cm<sup>2</sup> is employed, which has spatiotemporal widths  $w_x = 2\lambda_{\text{ST}}$  and  $w_t = 2T_{\text{ST}}$  ( $T_{\text{ST}} = 2\pi/\omega_{\text{ST}}$ ), respectively. It should be noted that  $w_x$  and  $w_t$  are not directly related to the actual beam spatial distribution or the pulse duration. These quantities are more like the beam waist of traditional light beams. From Fig. 1(b), it can be seen that the STOV pulse is distributed in a range of about  $\approx 13$   $\mu\text{m}$  (i.e.,  $\approx 8$  wavelengths), and the pulse lasted for more than 40 fs ( $\approx 8$  cycles). As shown in Fig. 1(b), the forked pattern in the center is the embodiment of the spatiotemporal singularity. In addition, the oscillation frequency of the electric field at different positions changes slightly, i.e., the STOV is spatially chirped. This is a consequence of the phase circulation [45].

To uncover the influence of the STOV spatiotemporal structure in strong field ionization, we assist the ionization with an XUV pulse, i.e., the electrons are first transferred to a highly excited state by the XUV pulse before being ionized by the STOV pulse, with a central wavelength of 91.13 nm ( $\omega_{\text{XUV}} = 0.5$  a.u.) and peak intensity  $I_{\text{XUV}} = 1 \times 10^{13}$  W/cm<sup>2</sup>. In this way, we can control the ionization time and position of the photoelectrons by changing the time delay and position of the XUV pulse relative to the STOV pulse,

as shown in Fig. 1(a) (violet dashed curve). The latter is experimentally feasible because the spatial size of a focused XUV pulse is much smaller than that of the STOV pulse. The XUV pulse can be written as

$$\mathbf{F}_{\text{XUV}}(t; \tau) = F_0^{\text{XUV}} f(t + \tau) \cos[\omega_{\text{XUV}}(t + \tau)] \hat{x}, \quad (2)$$

where  $\tau$  is the time delay relative to the spatiotemporal singularity,  $F_0^{\text{XUV}}$  is the peak electric field strength, and  $f(t)$  is the pulse envelope, which has a  $\cos^2(\pi t/T_p)$  shape with a duration of  $T_p = 32T_{\text{XUV}}$  ( $T_{\text{XUV}} = 2\pi/\omega_{\text{XUV}}$ ). The time delay is taken to be  $\tau_+ = w_t \sqrt{|l|/2}$  ( $\tau_+ = 7.62$  fs and 10.79 fs for  $l = 1$  and  $l = 2$ ) or  $\tau_- = -w_t \sqrt{|l|/2}$ , which corresponds to XUV pulses arriving before or after the spatiotemporal singularity, respectively [see the dashed lines in Fig. 1(b)]. The position of the XUV pulse in the  $x$  axis scans over a region from  $-1.6 w_x \sqrt{|l|/2}$  to  $1.6 w_x \sqrt{|l|/2}$  ( $-3.62$  to  $3.62$   $\mu\text{m}$  for  $l = 1$ , and  $-5.12$  to  $5.12$   $\mu\text{m}$  for  $l = 2$ ). Here,  $\pm w_t \sqrt{|l|/2}$  is the time when the electric field of the STOV pulse at position  $x = 0$  reaches its maximum, and  $\pm w_x \sqrt{|l|/2}$  is the position where the electric field at time  $t = 0$  reaches its maximum. If the XUV pulse comes first, electrons at a given position can be transferred to a highly excited state at a given time and then ionized by the STOV pulse. These electrons thus encode spatiotemporal information of the STOV.

### A. Numerically solving the time-dependent Schrödinger equation

The dynamics of an atomic electron interacting with strong laser pulses are governed by the 3D-TDSE. In the velocity gauge, it can be written as

$$i \frac{\partial \Psi(\mathbf{r}, t)}{\partial t} = \left( \frac{\mathbf{p}^2}{2} + \mathbf{A}_{\pm}^l(t, x) \cdot \mathbf{p} + V(\mathbf{r}) \right) \Psi(\mathbf{r}, t), \quad (3)$$

where  $V(\mathbf{r}) = -1/|\mathbf{r}|$  is the Coulomb potential of the H atom. Note that in Eq. (3) we have neglected the  $[\mathbf{A}_{\pm}^l(t, x)]^2$  term [48]. It contributes to a phase that does not affect the observables. The vector potential of the total laser pulse is described by

$$\mathbf{A}_{\pm}^l(t, x) = \int [\mathbf{F}_{\text{XUV}}(t; \tau_{\pm}) + \mathbf{F}_{\text{ST}}^l(t, x, y = 0)] dt, \quad (4)$$

where  $\tau_{\pm}$  is the time delay of the XUV pulse before or after the spatiotemporal singularity and  $\mathbf{F}_{\text{ST}}^l(t, x, y = 0)$  is the electric field of the STOV at  $x$ , where  $x$  is the spatial location of the XUV pulse relative to the singularity of the STOV.

To solve the 3D-TDSE, the wave function  $\Psi(\mathbf{r}, t)$  is expanded in spherical harmonics  $Y_{lm}(\theta, \phi)$  as

$$\Psi(\mathbf{r}, t) = \sum_{l,m} \frac{R_{lm}(r, t)}{r} Y_{lm}(\theta, \phi). \quad (5)$$

Here,  $R_{lm}(r, t)$  is the radial part of the wave function, which is discretized by the finite-element discrete variable representation method [49,50]. In our simulation, the angular momentum  $l$  is chosen up to 30 to guarantee convergence, the magnetic momentum  $m$  is taken to be 0 due to the linearly polarized character of both the STOV and XUV pulses, and the box size for the radial coordinate is  $r_{\text{max}} = 500$  a.u. The time-propagated electron wave function is obtained by the split-Lanczos method with a time step  $\Delta t = 0.1$  a.u. [51].

In each step of the time propagation, we use an absorbing mask function  $F(r) = 1 - 1/[1 + e^{(160-r)/2}]$  to split the wave function  $\Psi(\mathbf{r}, t)$  into an inner part  $\Psi_{\text{in}}(\mathbf{r}, t) = F(r)\Psi(\mathbf{r}, t)$  and an outer part  $\Psi_{\text{out}}(\mathbf{r}, t) = [1 - F(r)]\Psi(\mathbf{r}, t)$ . The inner part  $\Psi_{\text{in}}(\mathbf{r}, t)$  is evolved by the full 3D-TDSE, while the outer wave function is propagated by a Coulomb-Volkov propagator [52]. The initial wave function is prepared by imaginary-time propagation. This scheme is preferable for more complex atomic targets, where analytical solutions are not available. Thus, for any given Coulomb-like potential and quantum number, its associated ground-state wave function can be easily obtained (and excited states can be recovered as well, using orthonormalization tools). Since we normally simulate strong-field dynamics for complex atoms, typically constrained by experiments, we tend to use the imaginary-time propagation to obtain the initial wave function, even for the case of an H atom. Here, we chose the ground state of the H atom as the initial electronic state. The PMDs are then obtained by projecting the final wave function on the scattering states of the H atom.

In our analysis, spin-orbit coupling is not considered. This is because (i) the ponderomotive energy  $U_p$  (of both the STOV and XUV pulses) is much smaller than the rest mass energy of an electron and (ii) we employ an H atom as a target, where spin effects are negligible.

### B. Semiclassical simulations

Although the laser-matter interaction processes can be adequately described by the 3D-TDSE, other methods are required to unfold the ultrafast electron dynamics. In this paper, to uncover the underlying physics of the interference patterns in the PMD, we resort to the SFA model [46,53–58]. Within this approach, such interference patterns are understood in terms of the quantum interference between different electron trajectories. In our calculations, due to the low intensity of the STOV, only the electron that is first promoted to a highly excited state by the XUV pulse can then be subsequently ionized by the weak STOV pulse. Thus, neglecting the rescattering process, the accumulated phase of the photoelectron is determined by the classical action  $S(x_0, t_{is})$  (note that only the STOV pulse should be taken into account):

$$S(x_0, t_{is}) = \frac{1}{2} \int_{t_{is}}^{t_e} dt' [\mathbf{p} + \mathbf{A}_{\text{ST}}^l(t', x)]^2 - (t_e - t_{is})I_p. \quad (6)$$

Here,  $x_0$  indicates the location of the atom.  $t_{is}$  is the saddle point for the ionization time ( $s$  represents the  $s$ th saddle point),  $t_e$  is the end of the laser pulse,  $\mathbf{A}_{\text{ST}}^l(t, x_0) = \int \mathbf{F}_{\text{ST}}^l(t', x_0) dt'$  is the vector potential, and  $I_p$  is the binding energy of the excited state from where the photoelectron is freed to the continuum (see the next section for details). For each given final momentum, the corresponding saddle-point equation is written as

$$\frac{1}{2} [\mathbf{p} + \mathbf{A}_{\text{ST}}^l(t_{is}, x_0)]^2 + I_p = 0. \quad (7)$$

Electrons ionized at different times but achieving the same final momentum can interfere with each other in the PMD, giving rise to interference structures. The PMD can be

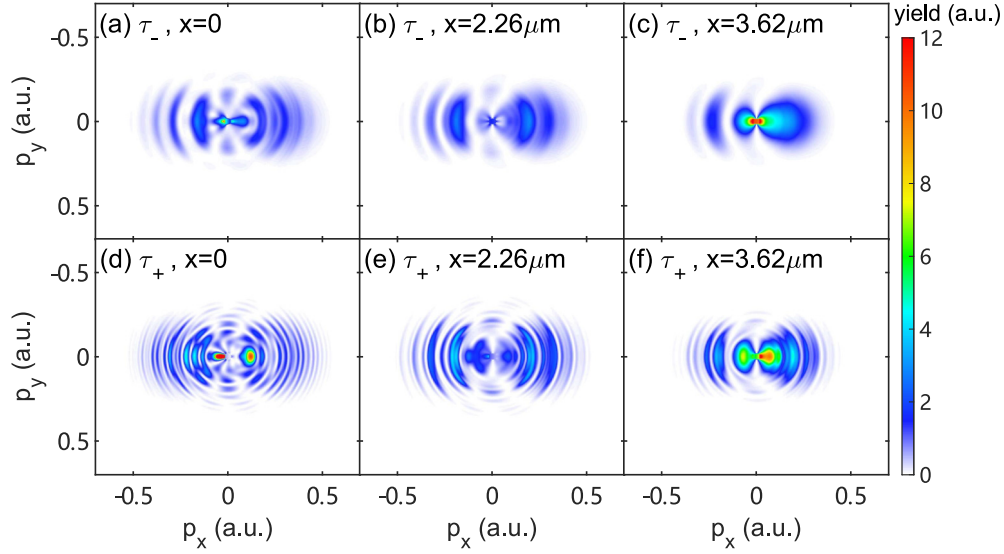


FIG. 2. PMDs for the photoionization of an H atom by a STOV pulse assisted by an XUV pulse. The STOV has a topological charge  $l = 1$ . (a)–(c) PMDs at positions  $x = 0$ ,  $x = w_x \sqrt{|l|/2}$  (2.26  $\mu\text{m}$ ) and  $x = 1.6 w_x \sqrt{|l|/2}$  (3.62  $\mu\text{m}$ ) for a negative time delay  $\tau_-$  of the XUV pulse. (d)–(f) PMDs at positions  $x = 0$ ,  $x = w_x \sqrt{|l|/2}$  and  $x = 1.6 w_x \sqrt{|l|/2}$  for a positive time delay  $\tau_+$  of the XUV pulse.

computed from

$$M(\mathbf{p}, x_0) = \left| \sum_s M_s(\mathbf{p}, x_0) e^{-iS(x_0, t_{is})} \right|^2, \quad (8)$$

where  $M_s(\mathbf{p}, x_0) e^{-iS(x_0, t_{is})}$  represents the transition amplitudes of electrons ionized at different times  $t_{is}$ . In this semiclassical model, the role of the XUV pulse is to control the ionization time and position of the direct electrons. Thus, the time delay  $\tau$  determines the range of ionization times: only electrons excited by the XUV pulse could be subsequently ionized by the STOV pulse. Here,  $t_{is} \in [\tau, t_e]$  should be considered. Moreover, the location  $x_0$  dictates the electric field shape of the STOV pulse  $\tilde{F}_{\text{ST}}^l(t', x_0)$  felt by the electrons.

### III. RESULTS AND DISCUSSION

In Fig. 2, we show the PMDs for the photoionization by a STOV pulse assisted by an XUV pulse of an H atom at different positions, namely,  $x=0$ ,  $x=w_x \sqrt{|l|/2}$  (2.26  $\mu\text{m}$ ) and  $x=1.6 w_x \sqrt{|l|/2}$  (3.62  $\mu\text{m}$ ) for  $l=1$ . The PMDs are plotted in the  $(p_x, p_y)$  plane ( $p_z=0$ ). Figures 2(a)–2(c) show the PMDs of electrons assisted by the XUV pulse with negative time delays  $\tau_-$ , i.e., the XUV pulse arrives after the spatiotemporal singularity. In this case, clear above-threshold ionization (ATI) peaks are visible. In addition, these PMDs are asymmetric along the laser polarization direction, which is due to the carrier-envelope phase (CEP) of the STOV pulse. Particularly in Fig. 2(c), where the effective interaction time of the STOV pulse with the atom is short, the CEP effect is more evident. In Figs. 2(d)–2(f), we show the PMDs for positive time delays  $\tau_+$  (here the XUV pulse comes before the spatiotemporal singularity). In this case, the electrons are excited by the XUV pulse before the singularity of the STOV pulse, and the PMDs exhibit additional interference structures. As the ionization

position of the photoelectron moves away from  $x = 0$  (i.e., the position of the spatiotemporal singularity), these interference fringes become sparse. The spatially resolved Fourier transform of the electric field of the STOV can be written as

$$\tilde{F}_{\text{ST}}^l(\omega, x) = \int F_{\text{ST}}^l(t, x) \exp(i\omega t) dt. \quad (9)$$

Here, the spectral weight of each frequency at different positions is given by  $|\tilde{F}_{\text{ST}}^l(\omega, x)|$ . In the inset of Fig. 3(a),

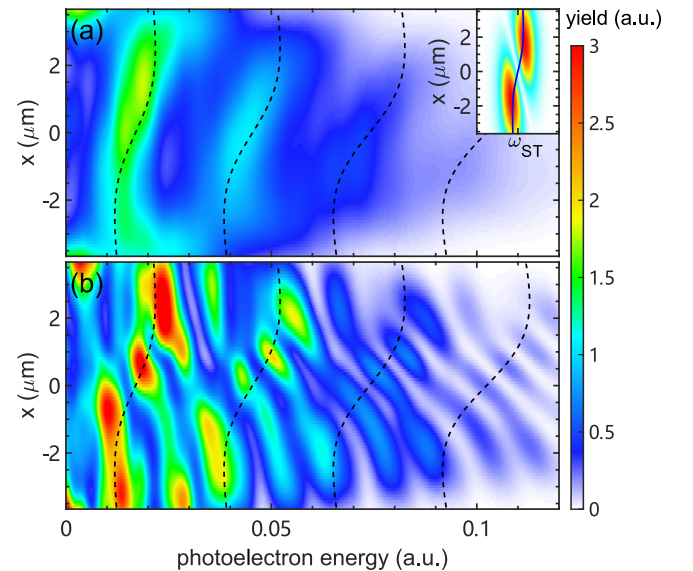


FIG. 3. Spatially resolved photoelectron energy spectra for time delays (a)  $\tau_-$  and (b)  $\tau_+$  of the XUV pulse obtained by the 3D-TDSE. The topological charge of the STOV is  $l = 1$ . The black dashed curves are the values of  $E_{1,2,3,4}^1(x)$  from Eq. (11). Inset: Spatially resolved frequency spectrum  $|\tilde{F}_{\text{ST}}^l(\omega, x)|$  of the electric field of the STOV pulse with  $l = 1$ . The solid blue curve is  $\omega^1(x)$  from Eq. (10).

we show the distribution of  $|\tilde{F}_{\text{ST}}^l(\omega, x)|$ . Then, the local carrier frequency, or the local photon energy, can be obtained by

$$\begin{aligned}\omega^l(x) &= \frac{\int |\tilde{F}_{\text{ST}}^l(\omega, x)| \omega d\omega}{\int |\tilde{F}_{\text{ST}}^l(\omega, x)| d\omega} \\ &= \omega_{\text{ST}} + \Delta\omega^l(x).\end{aligned}\quad (10)$$

Here,  $\Delta\omega^l(x)$  is the frequency variation caused by the spatiotemporal phase circulation. The spatial change in the local carrier frequency  $\omega^l(x)$  is known as the spatial chirp of the STOV pulse [45], which results in a spatial varying ATI spectrum. We plot  $\omega^l(x)$  as a solid blue curve in the inset of Fig. 3(a). It can be seen that the spatial change of  $\omega^l(x)$  follows the trend of the visible twist in the ATI spectra (see below for more details).

In Fig. 3(b), we show the spatially resolved spectrum for time delays  $\tau_+$ . A set of tilted interference fringes can be clearly seen now. A similar structure has been recently reported in a theoretical work about HHG [45]. For positive time delays  $\tau_+$ , the electron is transferred to an excited state before the singularity and is then ionized by the STOV pulse. This ionization occurs both before and after the spatiotemporal singularity. This fact gives rise to the interference pattern visible in Fig. 3(b). It can be considered as a *temporal* double-slit interference. In the case of negative time delays  $\tau_-$  in Fig. 3(a), the electrons are ionized only after the singularity, and thus the interference fringes disappear. We can conclude then that these fringes are associated with the interference between electrons ionized before and after the singularity with the same momentum (energy). Interestingly, the number of interference fringes increases with the photoelectron energy. This is related to the number of absorbing photons per electron, as we detail next.

To unfold the origin of these interference fringes more clearly, we employ the SFA. Figure 4 shows the spatially resolved photoelectron energy spectra obtained from the SFA for the STOV pulse with  $l = 1$ . Here, the electrons are ionized from the  $4p$  state of the H atom (see below for more details). In Fig. 4(a), we show a spatially resolved photoelectron energy spectrum for electrons ionized within the time range  $[-\tau_+, t_e]$ , that corresponds to the case of an XUV pulse with positive time delay  $\tau_+$ . We can observe that the result from the SFA agrees very well with the 3D-TDSE simulations [Fig. 3(b)]. In our SFA calculations, we can separately calculate spatially resolved photoelectron energy spectra for electrons released before and after the singularity  $t=0$ . Figures. 4(b) and 4(c) show the spatially resolved spectra for electrons ionized by the STOV pulse within the time ranges  $[-\tau_+, 0]$  and  $[0, t_e]$ , respectively. Here, the interference fringes on the ATI spectra are absent in each of the individual contributions. Contrariwise, in the coherent sum of these two spectra, the twisted interference structures are clearly visible [Fig. 4(a)], which are similar to those present in Fig. 3(a). This definitely indicates that the interference fringes result from the interference between the electrons ionized before and after the spatiotemporal singularity.

The interference pattern in the spatially resolved photoelectron energy spectra encodes the phase of the laser-ionized

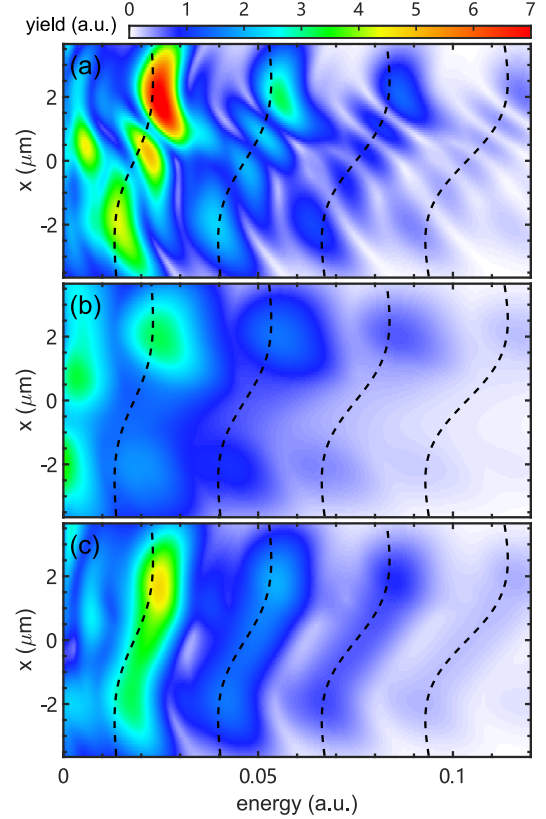


FIG. 4. Spatially resolved photoelectron energy spectrum calculated by the SFA for a STOV pulse with  $l = 1$ .  $I_p = 0.0325$  a.u. is the binding energy of the  $4p$  state of the H atom. (a) For electrons ionized before and after the spatiotemporal singularity, i.e.,  $t_{is} \in [-\tau_+, t_e]$ . (b) For electrons ionized before the spatiotemporal singularity, i.e.,  $t_{is} \in [-\tau_+, 0]$ . (c) For electrons ionized after the spatiotemporal singularity, i.e.,  $t_{is} \in [0, t_e]$ . The black dashed curves are the values of  $E_{1,2,3,4}^1(x)$  from Eq. (11).

photoelectron, acquired during its journey in the continuum. When the STOV pulse interacts with the atom, the temporal structure of the phase of the STOV pulse is recorded in the photoelectrons ionized before and after the singularity. The quantum interference between these two trajectories followed by the photoelectrons thus can be used to retrieve the temporal structure of the STOV pulse. In addition, the phase difference between them depends on the position where the ionization occurs. This difference is related to the spatial structure of the STOV pulse. By analyzing the interference pattern as a function of the spatial location of the XUV pulse relative to the singularity, the spatiotemporal structure of the STOV pulse, i.e., the OAM, can be fully characterized.

From the discussion above, we can infer that the transverse OAM transfer is echoed in the interference pattern visible in the spatially resolved photoelectron energy spectrum. The inset of Fig. 3(a) shows the spatially resolved frequency spectrum of the STOV pulse. One minimum in the interference pattern is clearly visible, which can be linked to the topological charge value of the STOV,  $l = 1$ . Analogous to the OAM transfer in HHG [30,43–45], when the electron is ionized by absorbing one photon, the photoelectron spectrum possesses

topological charge of  $l = 1$ , and one interference dark fringe will appear. When the number of absorbed photons increases by one, so does the topological charge. In Fig. 3(b), the first-order ATI spectrum has two dark fringes along the dashed line, meaning that in this part it has a topological charge  $l = 2$ . Thus, this indicates that the electron has absorbed two photons from the STOV pulse to get ionized from the excited state. Likewise, for the second- or third-order ATI spectra, the topological charge becomes  $l = 3$  or  $l = 4$ , respectively. This is reflected in the number of interference fringes in the corresponding ATI spectrum see Fig. 3(b)]. However, for the negative delay, all the electrons are ionized after the singularity. In this case, only a part of the OAM is transferred from the photons to the electrons. Thus the spatially resolved ATIs spectra miss the information on the temporal structure of the OAM, and the interference fringes disappear, as shown in Fig. 3(a).

From the number of the interference dark fringes, one could extract the number of photons from the STOV pulse that the electron absorbs. Then, we can estimate the excited state from which the photoelectron is released. For the  $n$ th order ATI spectrum, the energy is given by

$$E_n^l(x) = (n + 1)\omega^l(x) - U_p^l(x) - I_p, \quad (11)$$

where  $U_p^l(x) = (F_0^{\text{ST}}/2\omega^l(x))^2$  is the ponderomotive energy of the STOV at position  $x$ , and  $I_p$  is the binding energy of the excited state. In Fig. 3(a),  $\omega^1(0) = 0.0285$  a.u. (for 1600 nm),  $U_p^1(0) = 0.0088$  a.u., and the energy of the first-order ATI spectrum at  $x = 0$  is about 0.0157 a.u. Thus, an  $I_p = 0.0325$  a.u. is obtained, which is close to the binding energy of the  $4p$  state of the H atom. This means that the electrons are first transferred to this excited state by the XUV pulse and then ionized by the STOV pulse. Taking the  $4p$  state as the initial state where the electron is ionized by the STOV pulse, we plot  $E_{1,2,3,4}^1(x)$  in Figs. 3 and 4 (dashed black curves). These curves agree very well with each of the ATI spectra. Particularly, the degree of spatial chirp is similar for the dashed curves and the TDSE results at each ATI spectrum. Likewise, the interference fringes are distributed along these curves.

To further explore the influence of the OAM of the STOV pulse on the interference structure, we calculate the spatially resolved photoelectron energy spectra for a STOV pulse with  $l = 2$ . The results are shown in Figs. 5(a) and 5(b), which are obtained from the 3D-TDSE and SFA, respectively. Taking into account the degree of approximation considered in the SFA—the influence of the Coulomb potential is neglected for electrons in the continuum in this approach—it can be seen that these two results agree very well. For this case, the interference fringes become denser at each ATI spectra (along the dashed curves), as compared to those for  $l = 1$ . Taking into account that the topological charge is  $l = 2$  in Fig. 5, the first-, second-, and third-order ATI spectra, which come from the electrons absorbing two, three, and four photons, have topological charges of  $l = 4, 6, 8$ , respectively. Likewise, the number of interference fringes increases accordingly. To observe this last feature more clearly, in Figs. 6(a) and 6(b) we show the fringes along  $E_3^l(x)$  [see Eq. (11)] for  $l = 1$  and  $l = 2$ , respectively. The agreement between the 3D-TDSE and

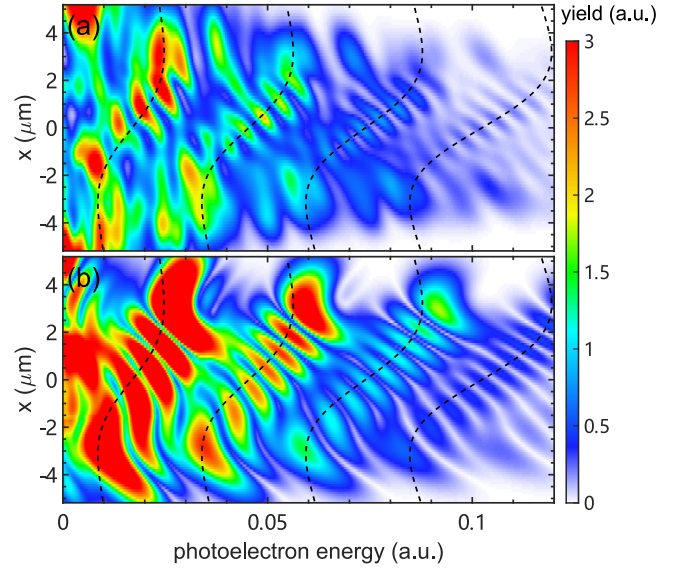


FIG. 5. Spatially resolved photoelectron energy spectrum for a STOV pulse with  $l = 2$  and an XUV pulse with time delay  $\tau_+$ . (a) 3D-TDSE results, (b) SFA results. The black dashed curves are the values of  $E_{1,2,3,4}^1(x)$  from Eq. (11).

SFA results is remarkable for both cases. For the same order of the ATI spectrum, the interference fringes are different for  $l = 1$  and  $l = 2$ . Here, the electron absorbs four photons from the STOV pulse. Thus, the topological charges are  $l = 4$  and  $l = 8$ , respectively, and the spectra should exhibit four and eight minima, i.e., interference dark fringes. This behavior is clearly noticeable in Fig. 6. Therefore, the spatiotemporal structure of the STOV pulse is encoded by the interference structures. Consequently, from the interference pattern in the spatially resolved photoelectron energy spectrum, we can retrieve the transfer of the transverse OAM in atomic strong-field ionization.

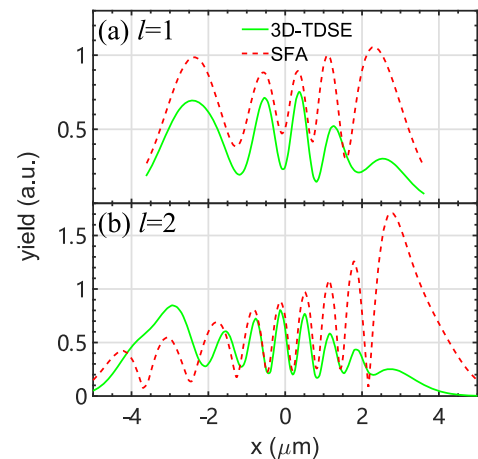


FIG. 6. Interference fringes along  $E_3^l(x)$  (Eq. 11) for (a)  $l = 1$  and (b)  $l = 2$ . The green solid and red dashed curves represent the 3D-TDSE and SFA results, respectively.

#### IV. CONCLUSIONS

In this paper, we have presented a technique to characterize a STOV. Our approach extends the well-known streaking technique, used to fully characterize the electric fields of infrared pulses with attosecond time resolution, to a more complex scenario. The field shape of a STOV is much more complex, having variations both in time and space. Taking advantage of the strongly nonlinear nature of strong field ionization, we can extract both the temporal and spatial information of the STOV electric field using photoelectrons. One of the main characteristics of the STOV is that it carries a transverse OAM. In our scheme, based on an XUV-assisted ionization, this intrinsic property of the STOV becomes encoded in the spatially resolved photoelectron spectra. Using both quantum mechanical and semiclassical-based simulations, we are able to accurately retrieve the OAM of the STOV, just by counting the number of fringes in an interferencelike pattern. Our results present a route toward (i) the extension of streaking techniques to the spatial domain and (ii) a more complete

understanding of the electron dynamics driven by a STOV, where the transverse OAM appears to play an instrumental role.

#### ACKNOWLEDGMENTS

This work was supported by the National Key Research and Development Program of China (Grant No. 2019YFA0308300) and the National Natural Science Foundation of China (Grants No. 11874163 and No. 12021004). M.F.C. acknowledges financial support from the Guangdong Province Science and Technology Major Project (Future functional materials under extreme conditions, No. 2021B0301030005) and the Guangdong Natural Science Foundation (General Program project, No. 2023A1515010871). The computing work in this paper is supported by the Public Service Platform of High-Performance Computing provided by the Network and Computing Center of HUST.

- 
- [1] L. Allen, M. W. Beijersbergen, R. J. C. Spreeuw, and J. P. Woerdman, Orbital angular momentum of light and the transformation of Laguerre-Gaussian laser modes, *Phys. Rev. A* **45**, 8185 (1992).
  - [2] G. Molina-Terriza, J. P. Torres, and L. Torner, Twisted photons, *Nat. Phys.* **3**, 305 (2007).
  - [3] N. Chattaripiban, E. A. Rogers, D. Cofield, W. T. Hill, and R. Roy, Generation of nondiffracting Bessel beams by use of a spatial light modulator, *Opt. Lett.* **28**, 2183 (2003).
  - [4] A. T. O’Neil, I. MacVicar, L. Allen, and M. J. Padgett, Intrinsic and Extrinsic Nature of the Orbital Angular Momentum of a Light Beam, *Phys. Rev. Lett.* **88**, 053601 (2002).
  - [5] M. Padgett, J. Courtial, and L. Allen, Light’s orbital angular momentum, *Phys. Today* **57**, 35 (2004).
  - [6] Y. Zhao, J. S. Edgar, G. D. M. Jeffries, D. McGloin, and D. T. Chiu, Spin-to-Orbital Angular Momentum Conversion in a Strongly Focused Optical Beam, *Phys. Rev. Lett.* **99**, 073901 (2007).
  - [7] G. F. Quinteiro, and P. I. Tamborenea, Theory of the optical absorption of light carrying orbital angular momentum by semiconductors, *Europhys. Lett.* **85**, 47001 (2009).
  - [8] K. Y. Bliokh, F. J. Rodríguez-Fortuño, F. Nori, and A. V. Zayats, Spin-orbit interactions of light, *Nat. Photonics* **9**, 796 (2015).
  - [9] M. Li, Y. Cai, S. Yan, Y. Liang, P. Zhang, and B. Yao, Orbit-induced localized spin angular momentum in strong focusing of optical vectorial vortex beams, *Phys. Rev. A* **97**, 053842 (2018).
  - [10] Y. Shen, X. Wang, Z. Xie, C. Min, X. Fu, Q. Liu, M. Gong, and X. Yuan, Optical vortices 30 years on: OAM manipulation from topological charge to multiple singularities, *Light: Sci. Appl.* **8**, 90 (2019).
  - [11] M. Ritsch-Marte, Orbital angular momentum light in microscopy, *Philos. Trans. R. Soc. London A* **375**, 20150437 (2017).
  - [12] L. Gong, Q. Zhao, H. Zhang, X. Y. Hu, K. Huang, J. M. Yang, and Y. M. Li, Optical orbital-angular-momentum multiplexed data transmission under high scattering, *Light: Sci. Appl.* **8**, 27 (2019).
  - [13] M. Padgett, and R. Bowman, Tweezers with a twist, *Nat. Photonics* **5**, 343 (2011).
  - [14] L. Rego, K. M. Dorney, N. J. Brooks, Q. L. Nguyen, C.-T. Liao, J. S. Román, D. E. Couch, A. Liu, E. Pisanty, M. Lewenstein *et al.*, Generation of extreme-ultraviolet beams with time-varying orbital angular momentum, *Science* **364**, eaaw9486 (2019).
  - [15] Z. Zhou, C. Min, H. Ma, Y. Zhang, X. Xie, H. Zhan, and X. Yuan, Time-varying orbital angular momentum in tight focusing of ultrafast pulses, *Opt. Express* **30**, 13416 (2022).
  - [16] A. Picón, A. Benseny, J. Mompart, J. R. Vázquez de Aldana, L. Plaja, G. F. Calvo, and L. Roso, Transferring orbital and spin angular momenta of light to atoms, *New J. Phys.* **12**, 083053 (2010).
  - [17] A. Picón, J. Mompart, J. R. Vázquez de Aldana, L. Plaja, G. F. Calvo, and L. Roso, Photoionization with orbital angular momentum beams, *Opt. Express* **18**, 3660 (2010).
  - [18] C. T. Schmiegelow, J. Schulz, H. Kaufmann, T. Ruster, U. G. Poschinger, and F. Schmidt-Kaler, Transfer of optical orbital angular momentum to a bound electron, *Nat. Commun.* **7**, 12998 (2016).
  - [19] O. Matula, A. G. Hayrapetyan, V. G. Serbo, A. Surzhykov, and S. Fritzsche, Atomic ionization of hydrogen-like ions by twisted photons: angular distribution of emitted electrons, *J. Phys. B: At., Mol. Opt. Phys.* **46**, 205002 (2013).
  - [20] W. Paufler, B. Böning, and S. Fritzsche, Strong-field ionization with twisted laser pulses, *Phys. Rev. A* **97**, 043418 (2018).
  - [21] B. Böning, W. Paufler, and S. Fritzsche, Above-threshold ionization by few-cycle Bessel pulses carrying orbital angular momentum, *Phys. Rev. A* **98**, 023407 (2018).
  - [22] S. Giri, M. Ivanov, and G. Dixit, Signatures of the orbital angular momentum of an infrared light beam in the two-photon transition matrix element: A step toward attosecond chronoscopy of photoionization, *Phys. Rev. A* **101**, 033412 (2020).

- [23] I. N. Ansari, D. S. Jadoun, and G. Dixit, Angle-resolved attosecond streaking of twisted attosecond pulses, [arXiv:2006.01582](#).
- [24] A. Sen, A. Sinha, S. Sen, V. Sharma, and R. Gopal, Above-threshold ionization of argon with ultrashort orbital-angular-momentum beams, *Phys. Rev. A* **106**, 023103 (2022).
- [25] J. Wätzel and J. Berakdar, Electrons in intense laser fields with local phase, polarization, and skyrmionic textures, *Phys. Rev. A* **102**, 063105 (2020).
- [26] J. Wätzel, P. R. Ribič, M. Coreno, M. B. Danailov, C. David, A. Demidovich, M. Di Fraia, L. Giannessi, K. Hansen *et al.*, Light-Induced Magnetization at the Nanoscale, *Phys. Rev. Lett.* **128**, 157205 (2022).
- [27] G. D. Ninno, J. Wätzel, P. R. Ribič, E. Allaria, M. Coreno, M. B. Danailov, C. David, A. Demidovich, M. Di Fraia, L. Giannessi *et al.*, Photoelectric effect with a twist, *Nat. Photonics* **14**, 554 (2020).
- [28] Y. Fang, Z. Guo, P. Ge, X. Ma, M. Han, X. Yu, Y. Deng, Q. Gong, and Y. Liu, Strong-field photoionization of intense laser fields by controlling optical singularities, *Sci. China: Phys., Mech. Astron.* **64**, 274211 (2021).
- [29] Y. Fang, M. Han, P. Ge, Z. Guo, X. Yu, Y. Deng, C. Wu, Q. Gong, and Y. Liu, Photoelectronic mapping of the spin-orbit interaction of intense light fields, *Nat. Photonics* **15**, 115 (2021).
- [30] C. Hernández-García, A. Picón, J. S. Román, and L. Plaja, Attosecond Extreme Ultraviolet Vortices from High-Order Harmonic Generation, *Phys. Rev. Lett.* **111**, 083602 (2013).
- [31] G. Gariepy, J. Leach, K. T. Kim, T. J. Hammond, E. Frumker, R. W. Boyd, and P. B. Corkum, Creating High-Harmonic Beams with Controlled Orbital Angular Momentum, *Phys. Rev. Lett.* **113**, 153901 (2014).
- [32] L. Rego, J. S. Román, A. Picón, L. Plaja, and C. Hernández-García, Nonperturbative Twist in the Generation of Extreme-Ultraviolet Vortex Beams, *Phys. Rev. Lett.* **117**, 163202 (2016).
- [33] D. Gauthier, P. R. Ribič, G. Adhikary, A. Camper, C. Chappuis, R. Cucini, L. F. DiMauro, G. Dovillaire, F. Frassetto, R. Géneaux, P. Miotti *et al.*, Tunable orbital angular momentum in high-harmonic generation, *Nat. Commun.* **8**, 14971 (2017).
- [34] K. M. Dorney, L. Rego, N. J. Brooks, J. S. Román, C.-T. Liao, J. L. Ellis, D. Zusin, C. Gentry, Q. L. Nguyen, J. M. Shaw, A. Picón *et al.*, Controlling the polarization and vortex charge of attosecond high-harmonic beams via simultaneous spin-orbit momentum conservation, *Nat. Photonics* **13**, 123 (2019).
- [35] A. P. Sukhorukov and V. V. Yangirova, Spatio-temporal vortices: Properties, generation and recording, *Nonlinear Opt. Appl.* **5949**, 594906 (2005).
- [36] K. Y. Bliokh and F. Nori, Spatiotemporal vortex beams and angular momentum, *Phys. Rev. A* **86**, 033824 (2012).
- [37] K. Y. Bliokh and F. Nori, Transverse and longitudinal angular momenta of light, *Phys. Rep.* **592**, 1 (2015).
- [38] N. Jhajj, I. Larkin, E. W. Rosenthal, S. Zahedpour, J. K. Wahlstrand, and H. M. Milchberg, Spatiotemporal Optical Vortices, *Phys. Rev. X* **6**, 031037 (2016).
- [39] A. Chong, C. Wan, J. Chen, and Q. Zhan, Generation of spatiotemporal optical vortices with controllable transverse orbital angular momentum, *Nat. Photonics* **14**, 350 (2020).
- [40] S. W. Hancock, S. Zahedpour, A. Goffin, and H. M. Milchberg, Free-space propagation of spatiotemporal optical vortices, *Optica* **6**, 1547 (2019).
- [41] K. Y. Bliokh, Spatiotemporal Vortex Pulses: Angular Momenta and Spin-Orbit Interaction, *Phys. Rev. Lett.* **126**, 243601 (2021).
- [42] S. W. Hancock, S. Zahedpour, and H. M. Milchberg, Mode Structure and Orbital Angular Momentum of Spatiotemporal Optical Vortex Pulses, *Phys. Rev. Lett.* **127**, 193901 (2021).
- [43] S. W. Hancock, S. Zahedpour, and H. M. Milchberg, Second-harmonic generation of spatiotemporal optical vortices and conservation of orbital angular momentum, *Optica* **8**, 594 (2021).
- [44] G. Gui, N. J. Brooks, H. C. Kapteyn, M. M. Murnane, and C.-T. Liao, Second-harmonic generation and the conservation of spatiotemporal orbital angular momentum of light, *Nat. Photonics* **15**, 608 (2021).
- [45] Y. Fang, S. Lu, and Y. Liu, Controlling Photon Transverse Orbital Angular Momentum in High Harmonic Generation, *Phys. Rev. Lett.* **127**, 273901 (2021).
- [46] M. Lewenstein, P. Balcou, M. Y. Ivanov, A. L'Huillier, and P. B. Corkum, Theory of high-harmonic generation by low-frequency laser fields, *Phys. Rev. A* **49**, 2117 (1994).
- [47] K. Amini, J. Biegert, F. Calegari, A. Chacón, M. F. Ciappina, A. Dauphin, D. K. Efimov, C. F. de M. Faria, K. Giergiel, P. Gniewek *et al.*, Symphony on strong field approximation, *Rep. Prog. Phys.* **82**, 116001 (2019).
- [48] B. H. Bransden and C. J. Joachain, *Physics of Atoms and Molecules*, 2nd ed. (Prentice Hall, Englewood Cliffs, NJ, 2003).
- [49] T. N. Rescigno and C. W. McCurdy, Numerical grid methods for quantum-mechanical scattering problems, *Phys. Rev. A* **62**, 032706 (2000).
- [50] J. Liang, Y. Zhou, Y. Liao, W.-C. Jiang, M. Li, and P. Lu, Direct visualization of deforming atomic wavefunction in ultraintense high-frequency laser pulses, *Ultrafast Sci.* **2022**, 9842716 (2022).
- [51] W.-C. Jiang and X.-Q. Tian, Efficient Split-Lanczos propagator for strong-field ionization of atoms, *Opt. Express* **25**, 26832 (2017).
- [52] D. G. Arbó, J. E. Miraglia, M. S. Gravielle, K. Schiessl, E. Persson, and J. Burgdörfer, Coulomb-Volkov approximation for near-threshold ionization by short laser pulses, *Phys. Rev. A* **77**, 013401 (2008).
- [53] W. Becker, F. Grasbon, R. Kopold, D. Milošević, G. Paulus, and H. Walther, Above-threshold ionization: From classical features to quantum effects, *Adv. At. Mol. Phys.* **48**, 35 (2002).
- [54] D. B. Milošević and W. Becker, Role of long quantum orbits in high-order harmonic generation, *Phys. Rev. A* **66**, 063417 (2002).
- [55] J. Tan, Y. Zhou, M. He, Q. Ke, J. Liang, Y. Li, M. Li, and P. Lu, Time-resolving tunneling ionization via strong-field photoelectron holography, *Phys. Rev. A* **99**, 033402 (2019).
- [56] D. B. Milošević, G. G. Paulus, D. Bauer, and W. Becker, Above-threshold ionization by few-cycle pulses, *J. Phys. B: At., Mol. Opt. Phys.* **39**, R203 (2006).
- [57] J. Itatani, F. Quéré, G. L. Yudin, M. Y. Ivanov, F. Krausz, and P. B. Corkum, Attosecond Streak Camera, *Phys. Rev. Lett.* **88**, 173903 (2002).
- [58] M. Kitzler, N. Milosevic, A. Scrinzi, F. Krausz, and T. Brabec, Quantum Theory of Attosecond XUV Pulse Measurement by Laser Dressed Photoionization, *Phys. Rev. Lett.* **88**, 173904 (2002).